Exp Fluids (2007) 42:169–184
DOI 10.1007/s00348-006-0188-8

RESEARCH ARTICLE

Visualizations of the flow inside an open cavity at medium range Reynolds numbers

Thierry M. Faure · Panayotis Adrianos · François Lusseyran · Luc Pastur

Received: 14 February 2006 / Revised: 18 May 2006 / Accepted: 13 July 2006 / Published online: 29 November 2006

Abstract The interaction between a laminar boundary layer and an open cavity is investigated experimentally for medium range Reynolds numbers. Flow visualizations are carried out for three different observation directions in order to understand the spatial development of dynamical structures. In particular, synchronized visualizations in two parallel planes picture the transverse development of the flow. The study is conducted by changing the cavity aspect ratio, the Reynolds number and therefore the flow patterns inside the cavity. The issue is to emphasize the 3-D development of the flow. In particular, we show that the dynamical structures are not due to secondary shear layer instabilities.

Nomenclature

A	plate length upstream of the cavity
B	plate length downstream of the cavity
D	wind tunnel height
$Gö$	Görtler number
H	cavity height
k	wave number
L	cavity length
R	aspect ratio
r_c	curvature radius
Re	Reynolds number
S	wind tunnel span
t	time
U_c	convection velocity inside the cavity
U_e	external velocity
(x, y, z)	Cartesian coordinates
Δ	difference
δ	boundary layer thickness inside the cavity
δ_2	momentum thickness inside the cavity
Λ	dimensionless coefficient
λ	wavelength
v	kinematics viscosity

T. M. Faure (✉) · P. Adrianos · F. Lusseyran · L. Pastur
Laboratoire d'Informatique pour la Mécanique et les Sciences de l'Ingénieur, Unité Propre de Recherche 3251, Centre National de la Recherche Scientifique,
B.P. 133, 91403 Orsay Cedex, France
e-mail: thierry.faure@limsi.fr

T. M. Faure · P. Adrianos
Université Pierre et Marie Curie, Paris 6,
4 place Jussieu, 75252 Paris Cedex 05, France

L. Pastur
Université Paris-Sud, Paris 11, 91405 Orsay Cedex, France

1 Introduction

A boundary layer interacting with a cavity is a benchmark case for environmental applications (airflow in a canyon street), aeronautics (landing gear cavities, bomb holds), automobile aerodynamics (interaction between the flow and an air inlet or an opening roof...) or industrial applications (structural discontinuities) where the velocity over a rectangular cavity is relatively low. The dynamical behavior of the vortices inside the cavity is unsteady and shows small as well as large vortex structures and it can be thought that it is mainly driven by the boundary shear layer. On the one hand, full information has been provided on the rectangular cavity configuration for high velocities with compressible effect. On the other hand, very low

velocity and Stokes flows in the Reynolds number range 50–1,600 were studied for the removal of a contaminated fluid inside the cavity (Fang et al. 1999). However, the dynamics of the boundary between the external flow and the cavity behaves in a different way for moderate Reynolds numbers (1,150–10,670), and few publications are available in that case. For this Reynolds number range the interaction between a turbulent boundary layer and a cavity was explored with particle image velocimetry measurements in water tunnel (Lin and Rockwell 2001) for a maximum Reynolds number of 11,000, and for a Reynolds number of 10,000 with a horizontal top plate above the end of the cavity (Kuo and Chang 1998). A local periodic excitation was applied at the beginning of the cavity to understand its coupling with the shear layer dynamics (Kuo and Jeng 2003). The flow developing in a series of canyon streets has been investigated recently (Chang and Meroney 2003a, b; Dezsö-Weidinger 2003).

General features of the dynamics can be depicted as follows. Viscous diffusion between the external and cavity flow generates a region with steep gradients of streamwise velocity concentrating most of the vorticity (Huerre and Rossi 1998). This organized vorticity is impinging on the downstream cavity wall, creating an acoustic feedback loop for high velocity configurations (Rockwell 1983). Many studies concerning the sound generation of the interaction between a flow and a cavity have been conducted (Rockwell and Naudascher 1978; Komerath et al. 1987; Howe 2003). The first model of the radiated acoustic waves was established on experimental results for Mach numbers greater than 0.4 (Rossiter 1964). An improved analytical model of the discrete frequency oscillations was established over the Mach number range $0.8 \leq M \leq 3$, without empirical constants (Bilanin and Covert 1973). It was suggested that the simultaneous excitation of two or more discrete frequencies which are not harmonics corresponds to the simultaneous participation of two or more vortex sheet displacement modes. A simple analytical model, where no vortex shedding is observed, describes the features of pressure fluctuations (Heller and Bliss 1975). A mathematical model based on the coupling of the shear layer instabilities with the acoustic feedback was developed considering the shear layer thickness (Tam and Block 1978).

One of the first experimental descriptions devoted to the mixing layer over a deep cavity for a compressible subsonic flow has been investigated by Forestier et al. (2003), where coherent vortices were established in the shear layer. The acoustic tones due to the feedback mechanism were consistent with the Rossiter formulation. A large-eddy simulation was conducted for the same configuration, with a time-frequency analysis showing a temporal modulation of the Rossiter mode levels, resulting in a special form of intermittency with competitive energy exchanges between modes (Larchevêque et al. 2004). A mode beating phenomenon has been reported for a supersonic flow (Kegerise et al. 2004). In that case, it is known that acoustic waves couple to the hydrodynamic field so as to close the feedback loop. Direct numerical simulations showed a transition from a shear-layer mode for shorter cavities and lower Mach numbers, to a wake mode, for longer cavities and higher Mach numbers (Rowley et al. 2002). Pressure fluctuations were also measured in the transonic regime (Chung 2001). Schlieren images and acoustic pressure measurements have been obtained for a supersonic flow over a cavity with length to height ratio varying in the range 0.25–6.25 (Umesh Chandra and Chakravarthy 2005).

The moderate Reynolds number range was investigated recently with acoustic and velocity measurements (Chatellier et al. 2004). A linearized stability analysis has modelled the interface of the cavity with a vorticity layer. For the same velocity range, the influence of the upstream laminar or turbulent boundary layer was studied (Grace et al. 2004). Flow oscillations on an axisymmetric cavity drag were studied for low velocities inside a water tunnel (Gharib and Roshko 1987). The cavity height is found to have little influence on the oscillations as far as it is not the same order in magnitude as the upstream boundary layer thickness (Sarohia 1977).

For the same Reynolds number range, flow dynamics studies have been achieved on lid-driven cavities: the difference with the present case is the absence of a freely developing shear layer. Ghia et al. (1982) used a multi-grid method to simulate the flow inside a square lid-driven cavity, where a main vortex is developing along the whole length. Visualizations have been conducted by Koseff and Street (1984) with dye emission, with tiny particle seeding (Migeon 2002; Migeon et al. 2003) and comparisons with numerical simulations were carried out for the same measurements (Guermond et al. 2002).

This short analysis of the flow in an open cavity reveals the diversity of the approaches. A synthesis is obviously not yet of topicality. The present study relates to an aspect not well documented in the literature, that of transverse instabilities. The 3-D features of the flow are not responsible for the strong frequency modes, which is the reason why this approach has not been much studied. However, at moderate flow rates, transverse modulation of the swirl, strongly conditions

the exchanges between the cavity and the main flow. The present study focuses on flow visualizations on moderate Reynolds number range varying the length over height ratio of the shear-layer driven cavity. The aim is to address the following issues:

- Give the flow morphology with cavity aspect ratio and Reynolds number.
- Track the 2-D or 3-D spatial nature of the flow.
- Provide the time development of the flow features.
- Analyze whether the 3-D flow development in the cavity is caused by secondary shear layer instabilities.

2 Experimental set-up and apparatus

The airflow is generated by a centrifugal fan placed upstream of a settling chamber (Fig. 1a). The seeding particle injection is achieved by the fan inlet. An axial duct terminated with honeycomb and a contraction drives the flow toward the experimental facility, which consists of a test section containing a flat plate beginning with an elliptical leading edge, in order to fix the boundary layer origin. The length of the plate is A = 300 mm providing an established laminar boundary layer. To reduce light wall reflections, the whole test section is made of antireflection glass 2 mm in thickness. The cavity height is fixed to H = 50 mm and its span is S = 300 mm (Fig. 1b), the cavity ends in the span direction are the wind tunnel vertical walls. The cavity aspect ratio $R = L/H$ (length over height) is studied from 0.5 to 2 by step of 0.5 by moving the glass pieces consisting in the downstream wall of the cavity and the downstream plate which has a length B = 370 mm. At the wind tunnel outlet, the flow is rejected inside the experimental room. The Reynolds number, determined with the cavity length L and the upstream boundary layer external velocity U_e, varies from 1,150 to 10,670, corresponding to external velocities from 0.69 to 1.60 m/s. The external velocity is measured with laser Doppler velocimetry 102 mm upstream the cavity and 25.5 mm above the flat plate. This point of measurement is in the external flow sufficiently upstream of the cavity to avoid any perturbation from the instability developing above the cavity. The origin of the coordinate system is set at the upstream edge of the cavity at mid span, the x axis is the flow direction, the y axis is normal to the upstream wall where the boundary layer develops and the z axis is along the cavity span. It has been checked that the test

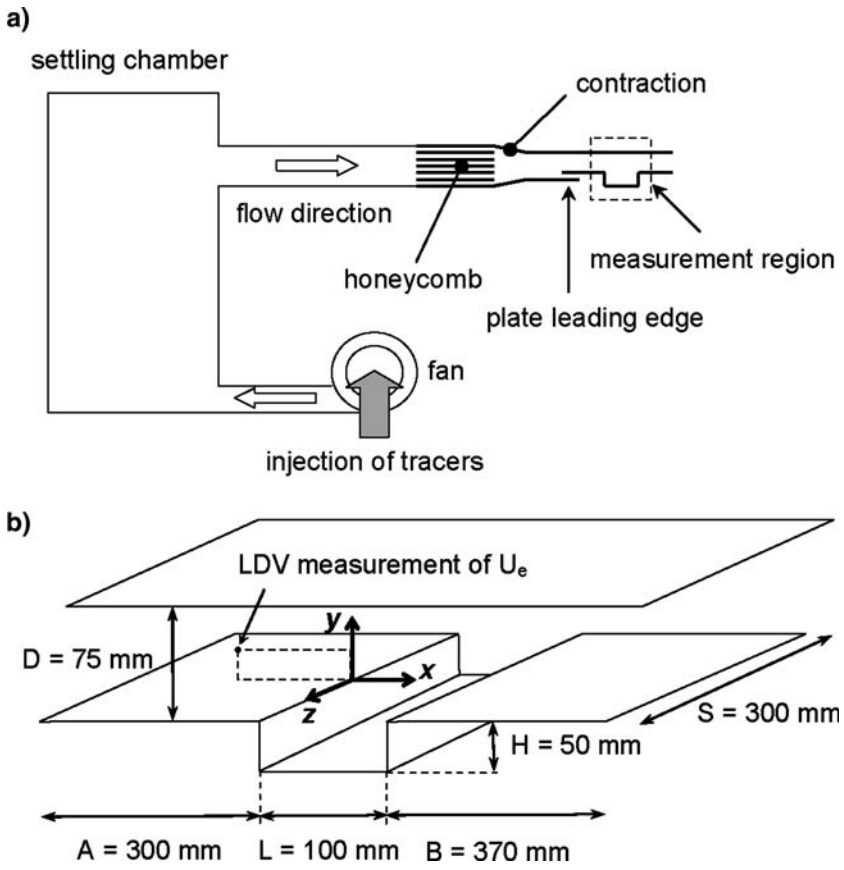

Fig. 1 Experimental set-up: **a** wind tunnel, **b** test section dimensions for R = 2 and coordinate system

section wall, located at $D = 75$ mm above the cavity, has no influence on the shear layer developing on the cavity. The thickness of the boundary layer developing on this wall is less than 10 mm and has no influence on the external flow along the longitudinal and spanwise directions. It has been shown for backward facing step flows that the influence of the upper wall affects the flow from 10 cavity heights downstream of the beginning of the step. The cavity under investigation is not a shallow cavity ($L/D > 5$), where the shear layer tends to attach the cavity floor (Geveci et al. 2003). However, in that configuration, the development and propagation of the large-scale vortices appear to be relatively unaffected by confinement effects. In the present study, it will be even more so given the maximum aspect ratio of 2.

Hereafter, the expressions ''upstream'' and ''downstream'' will refer to the external velocity direction. As smoke is used, the observed structures are emission lines of fluid injection inside the cavity and not the streamlines themselves. However, the flow injection inside the cavity gives information on the flow dynamics and the developing structures. Flow visualizations are carried out in different observation directions. The first configuration consists of two parallel planes (Fig. 2a). The light source is a 5 W argon-ion laser tuned to the blue (488 nm) and green (514.5 nm) wavelengths. The laser beams provide, by passing through cylindrical lenses, laser sheets which thickness is 0.25 mm. The blue laser sheet is settled in the middle of the span of the cavity ($z = 0$), the green one being moved along the span ($z = 30$ mm). A light trap is placed under the test section to remove any light scattering by the floor. The image recording system consists of two synchronized 8-bit cameras with $1{,}032 \times 778$ pixels and a frequency of 20 Hz. In order to make out only one wavelength by camera, two pass-band filters of appropriate frequencies are placed in front of the cameras. The magnification is the same for the two cameras, each one having a complete view of inside the cavity. Flow seeding is provided by a fog created with a low density smoke generator Starway Puffer One.

The second configuration visualizes a horizontal plane inside the cavity and uses the same system, with only one camera and the blue laser wavelength (Fig. 2b). The laser sheet position is counted from the upstream flat plate ($y = -15$ mm).

The third configuration provides observation in a transverse plane from downstream (Fig. 2c). The laser position x is taken from the upstream cavity edge, and set to the middle of cavity length ($x = L/2$).

The repeatability of flow visualizations has been checked by recording different image series with different wind tunnel runs, and by testing different smoke injections. The following section will present the flow dynamics in the three observation planes for each cavity aspect ratio considered. The external flow is

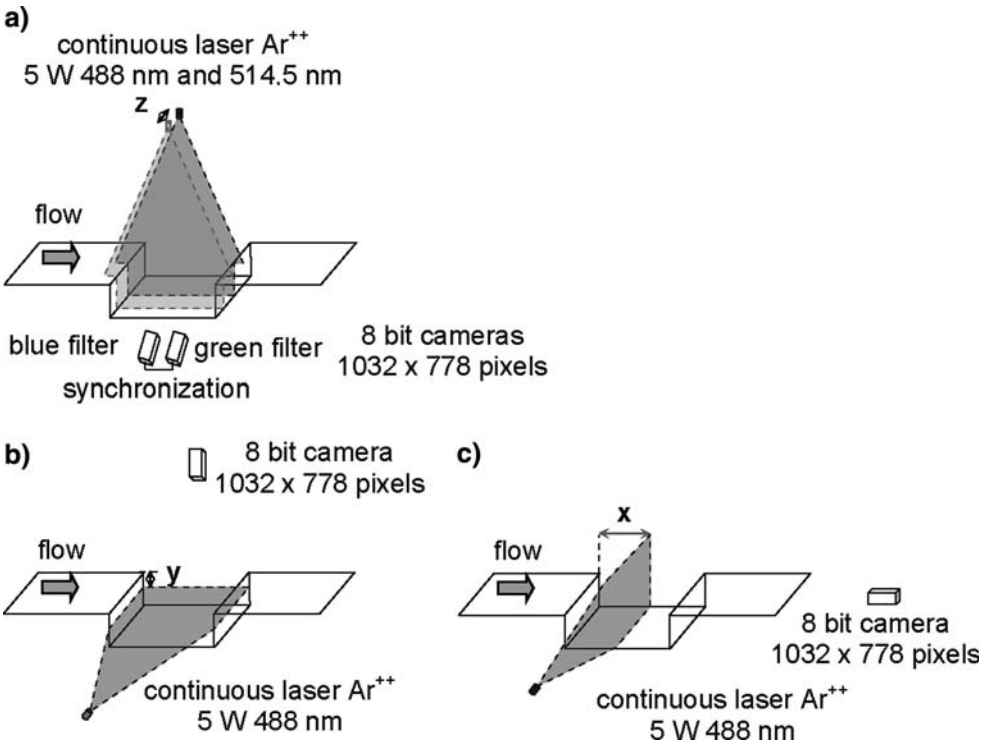

Fig. 2 Visualization planes: **a** two parallel vertical planes, **b** horizontal plane and **c** transverse plane

established and uniformly seeded with smoke when the images are recorded. Note that if the observation time is too long, there is a saturation of the cavity with smoke and no dynamical flow structure can be identified anymore.

3 Results

3.1 Aspect ratio $R = 2$

In the following figures, the view observed in the blue laser sheet, which is fixed in the middle span of the cavity ($z = 0$), is always presented on the left while the view observed in the green laser sheet ($z = 30$ mm) is on the right. The external flow direction is from left to right.

The best parameter to compare different flows could be the Reynolds number. However, the two space scales of the cavity (L and H) make the reduction of the flow properties impossible. Therefore, to provide a good understanding of the flow development with the velocity and aspect ratio, we have chosen to set a velocity and to vary the aspect ratio. Hereafter, the external velocity and Reynolds number are both provided in each figure caption.

Figure 3a shows the cavity flow for $U_e = 0.69$ m/s where the development and the oscillations of the shear layer are clearly identified by the boundary between the external flow, with a high smoke density and light levels, and the cavity flow with low smoke density and dark levels. The interaction between the shear layer and the downstream cavity edge leads to seeding injection inside the cavity that is not continuous, because of the shear layer oscillations. Note that the smoke pattern of the shear layer interaction with the downstream edge is similar in the two observation planes, which is evidence that this phenomenon could be 2-D. The seeding is advected inside the cavity as a mushroom like pattern. This pattern comes from the injection of the external flow inside the cavity. It originates from the shear layer oscillation near the downstream edge of the cavity and is similar to a jet pulsed flow. These successive patterns are advected inside a main vortex, which is filling the downstream part of the cavity. This vortex is developing in time and space, as it can be seen comparing its axial dimension between the middle cross-plane at $z = 0$ (Fig. 3a, left) and the plane situated at $z = 30$ mm (Fig. 3a, right) at the same time. The observation of the time records leads to the following comments. The vortex longitudinal modulation induces deformations of the patterns, which keep their coherence inside the vortex motion on a complete cycle. The interaction of the main vortex with the upstream part of the fluid inside the cavity creates a secondary counter-rotating vortex, which dimension is confined between the main vortex and the upstream cavity edge. This structure is highly time-dependant regarding the main vortex extension. The rotation of the two eddies generates an induced flow between them, confined by the cavity upstream wall and the shear layer. This induced flow has nowhere to develop except in the spanwise direction, leading to a transverse flow. Spanwise flows may exist inside the vortices cores, but are not clearly identified because of the lack of seeding.

Figure 3b is the same view of the flow for $U_e = 1.21$ m/s. The same dynamics is found, but for this time and $z = 30$ mm (Fig. 3b, right), the main vortex extension reaches the upstream edge, while the secondary vortex is limited to the bottom of the upstream edge. However, the seeding patterns are still well defined. A small counter-rotating secondary vortex is also identified at the bottom of the downstream wall corner.

Figure 3c presents the flow for $U_e = 1.60$ m/s with the same dynamics. Comparing this visualization with what is obtained for lower velocities (the right and left image in Fig. 3a, b, taken for the same time), note the fast smoke diffusion inside the cavity, reflected as a fog, caused by a higher turbulence level.

The axial extension of the main vortex fluctuates, leading to an alternated occupation of the upstream half of the cavity by the main or the secondary vortex. The fact that for two values of U_e and $z = 0$ (Fig. 3a, b, left) the main vortex takes up the downstream half of the cavity is fortuitous. Following in time this alternated occupation reveals that the spanwise modulation of these two vortices is not stationary.

In the top view plane shown in Fig. 4, the external flow is coming from the bottom of the figure. Figure 4 depicts the flow for $U_e = 1.21$ m/s and $y = -15$ mm below the flat plate inside the cavity, for four successive times. The image centering shows the whole cavity span. The two vertical white lines are the vertical visualization planes for $z = 0$ and $z = 30$ mm. The almost uniform white smoke strip at the downstream edge existing for time $t_0 + 0.1$ s (Fig. 4) is the smoke injection inside the cavity which confirms that it is mainly 2-D, except maybe near the span edges of the wind tunnel. The seeded parts of the cavity show patterns moving towards the top of the image (in the external flow direction), for the upper two third of the image, corresponding to the motion of the upper part of the main vortex. The spanwise modulation of this vortex is strongly time-dependant providing the presence of an unsteady flow inside the whole cavity. In the

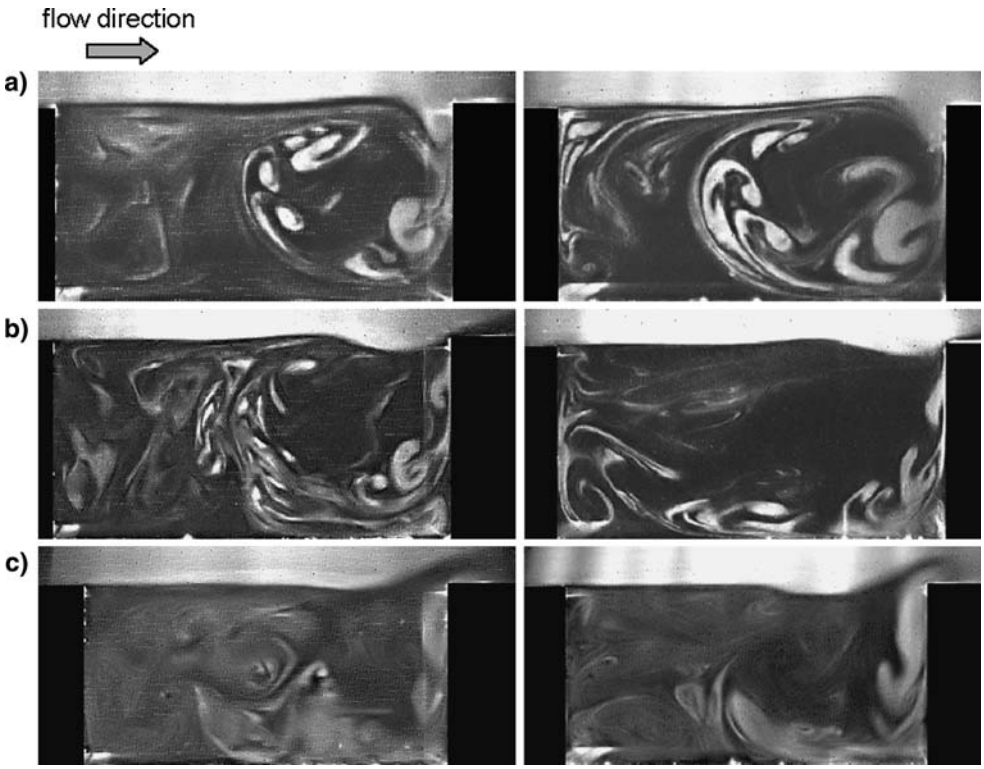

Fig. 3 Visualization in two parallel vertical planes (*left*: $z = 0$, *right*: $z = 30$ mm) for the same time and $R = 2$. **a** $U_e = 0.69$ m/s ($Re = 4{,}600$), **b** $U_e = 1.21$ m/s ($Re = 8{,}070$) **c** $U_e = 1.60$ m/s ($Re = 10{,}670$)

lower third of the image, smoke clusters are moving to the bottom, which indicates the motion of the secondary vortex. Destabilized pairs of unsteady counter-rotating vortices are also identified. In addition there is a spanwise flow near the upstream edge, resulting in the interaction of the fluid motion induced by the two vortices which is confined by the cavity edge and the shear layer, and forced to a lateral motion. As a result, the cavity flow looks fully 3-D.

For visualizations in the transverse plane, located in the middle of the cavity length (Fig. 5), the external flow is orthogonal to the figure pointing toward the reader. The view in this transverse plane shows the whole cavity span. The central white strip is a shadow zone where there is a reflection of the inner cavity flow: it is caused by the flow observation through the downstream flat glass plate, and has been removed in the image for clarity. First, we can notice, in the upper part of the image, the uniform smoke density of the laminar external flow, with the pattern of the honeycomb that is placed upstream of the wind tunnel contraction. The top and the bottom of the cavity are seeded while there is little smoke in the center: this corresponds to the main vortex motion. The lace-like pattern of the seeded regions indicates the deformation of the smoke lines injected uniformly along the span, caused by the main vortex motion inside the cavity. It reveals the main vortex motion of the 3-D flow development. These spanwise structures in the lower part of Fig. 4 might also be thought as Görtler-like vortices, but they are very unsteady and it is difficult to measure a wavelength. Moreover these structures are rapidly and repeatedly destroyed by the relatively high turbulence level inside the cavity.

Figure 6 sketches the flow dynamical structures for $R = 2$, with the external flow, the shear layer boundary which interacts with the downstream edge, the main vortex with a counter-rotating corner vortex, the secondary vortex, the flow induced by the vortices interaction and the resulting spanwise flow. In the central part of the span, the development of the shear layer and its interaction with the downstream wall are mostly 2-D but the flow is destabilized inside the cavity and gets 3-D features.

3.2 Aspect ratio $R = 1.5$

Similar analysis is achieved for aspect ratio $R = 1.5$. Figure 7a depicts, for $U_e = 0.69$ m/s the shear layer injection inside the cavity with smoke volutes advected inside the main vortex. Note for this velocity the very low smoke diffusion inside the cavity resulting in well defined marks for the injection patterns, which is an evidence of a lower turbulence level than for $R = 2$. The 3-D character of the fluid motion is observed by the differences between the two planes. The same flow

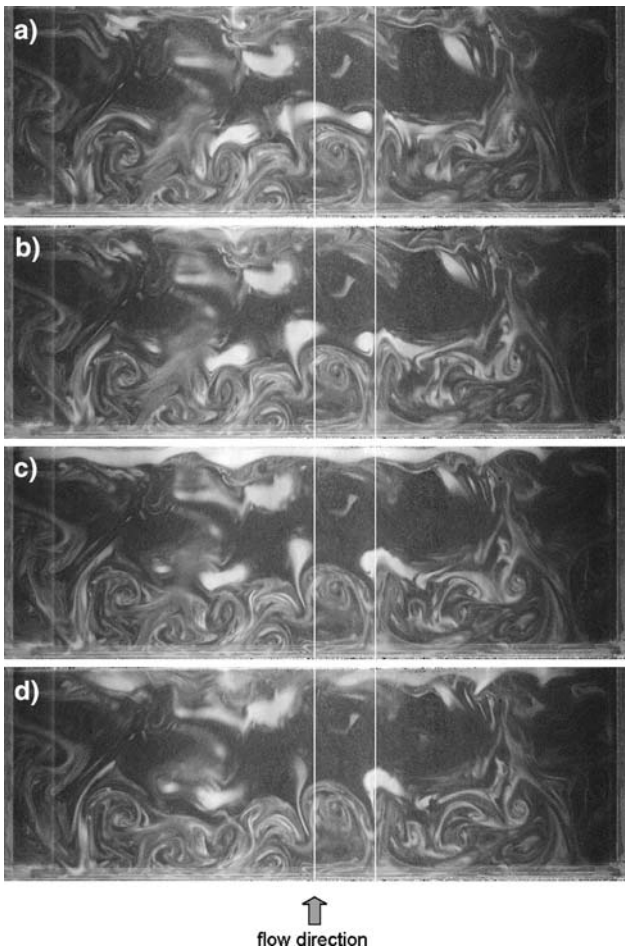

Fig. 4 Visualization in a horizontal plane for $R = 2$, $U_e = 1.21$ m/s ($Re = 8{,}070$) and $y = -15$ mm. **a** Time t_0, **b** time $t_0 + 0.05$ s, **c** time $t_0 + 0.1$ s, **d** time $t_0 + 0.15$ s

structure is found as for $R = 2$ with a main downstream vortex and a second counter-rotating upstream vortex. This secondary vortex is smaller than for $R = 2$ and is limited to the lower part of the cavity as it can be seen in the plane of visualization for $z = 30$ mm (Fig. 7, left) while the main vortex extension reaches, in the central plane ($z = 0$ mm), the upstream cavity wall. The mushroom-like patterns are less marked than for $R = 2$, this may be due to a lower momentum of flow injection inside the cavity.

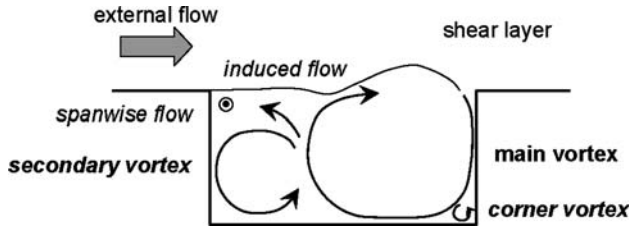

Fig. 6 Sketch of the cavity flow dynamics for $R = 2$

Figure 7b is the same view for $U_e = 1.21$ m/s. The same dynamics is found, but the smoke diffusion inside the main vortex is stronger and the volutes of seeding injection inside the cavity cannot be identified. Note at this particular time the secondary vortex extension limited to a corner in the central plane (Fig. 7b, left), while it is spreading in height in the second plane (Fig. 7b, right).

A similar behavior is observed for $U_e = 1.60$ m/s (Fig. 7c).

The flow visualizations in the horizontal plane are shown in Fig. 8, where the two white lines are the vertical visualization planes for $z = 0$ and $z = 30$ mm. The pairs of counter-rotating vortices are steadier than for $R = 2$ and are aligned along the upstream cavity wall. Flattened features are also present near the downstream cavity wall with the same spanwise periodicity. The central part of the flow is marked by a transverse flow from the span ends toward the centerline. The increase of the external velocity acts only on smoke diffusion and on the stability of the vortices.

Figure 9 is a sketch of the flow for $R = 1.5$, very similar to the vortices morphology found for $R = 2$.

3.3 Aspect ratio $R = 1$

For $R = 1$ the flow is only driven by one main vortex, spreading along the cavity length and height and induced by the shear layer oscillations which are lower than for the aspect ratios previously exposed (Fig. 10a). Two corner vortices are present at the bottom of the cavity as previously observed in a lid-driven cavity for a similar range of Reynolds numbers

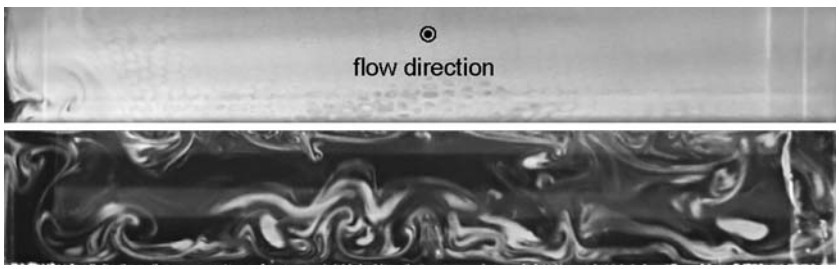

Fig. 5 Visualization in a transverse plane for $R = 2$, $U_e = 1.21$ m/s ($Re = 8{,}070$) and $x = L/2$

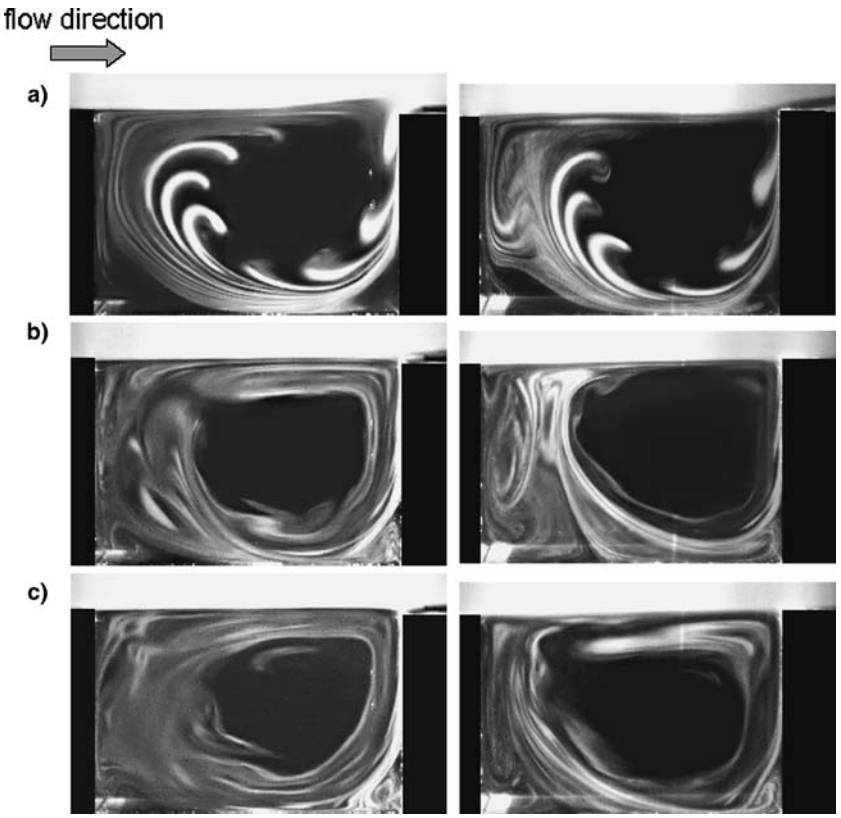

Fig. 7 Visualization in two parallel vertical planes (*left*: $z = 0$, *right*: $z = 30$ mm) for the same time and $R = 1.5$
a $U_e = 0.69$ m/s ($Re = 3{,}450$)
b $U_e = 1.21$ m/s ($Re = 6{,}050$)
c $U_e = 1.60$ m/s ($Re = 8{,}000$)

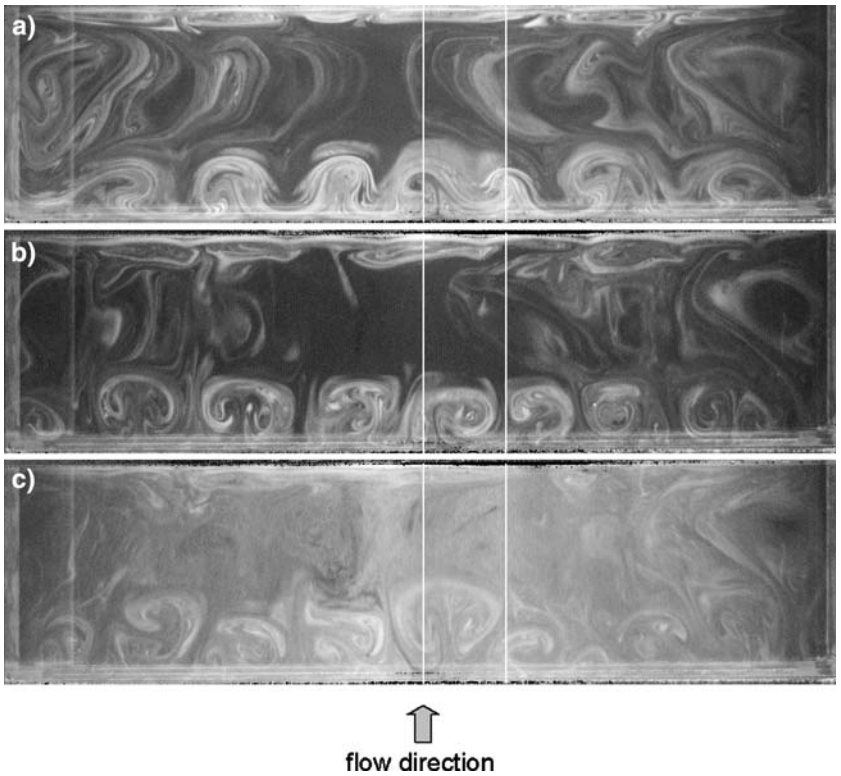

Fig. 8 Visualization in a horizontal plane for $R = 1.5$ and $y = -15$ mm.
a $U_e = 0.69$ m/s ($Re = 3{,}450$)
b $U_e = 1.21$ m/s ($Re = 6{,}050$).
c $U_e = 1.60$ m/s ($Re = 8{,}000$)

(Koseff and Street 1984). It appears that the upstream corner vortex is the development, for $R = 1$, of the secondary vortex existing for $R = 2$ and 1.5. As the main vortex, containing most of the flow energy, occupies the entire cavity length, there is no room for the counter-rotating eddy to develop, except in a

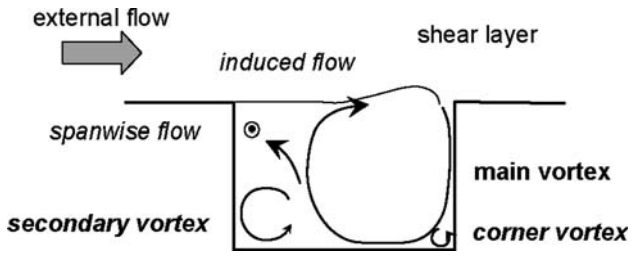

Fig. 9 Sketch of the cavity flow dynamics for $R = 1.5$

corner. Whatever the velocity is, the 3-D seems to be comparable (Fig. 10a–c). Moreover, the spanwise development in those two planes is not observable. The stretching is stronger with higher velocities as it can be seen by the alteration of the injection pattern into a sliced pattern.

The views of the flow inside a horizontal plane are shown in Fig. 11. The white lines are the vertical visualization planes for $z = 0$ and $z = 30$ mm (Fig. 11a–c). Note for $U_e = 0.69$ m/s (Fig. 11) that there is no undulated streamline flow pattern as it was found inside a square lid-driven cavity for almost the same Reynolds number (Migeon 2002). For $U_e \geq 1.21$ m/s, mushroom-like counter-rotating cells are observed at the bottom of the cavity near the upstream wall (Fig. 11b, c). Their transverse positioning in pairs is suggesting a development of Görtler vortices. Their origin can be related to the flow curvature induced by the main cavity vortex, which spreads over the entire cavity length and height. There is another structure, symmetric to each mushroom-like structure, located at the downstream cavity wall which can be understood as the same pattern, structured into a

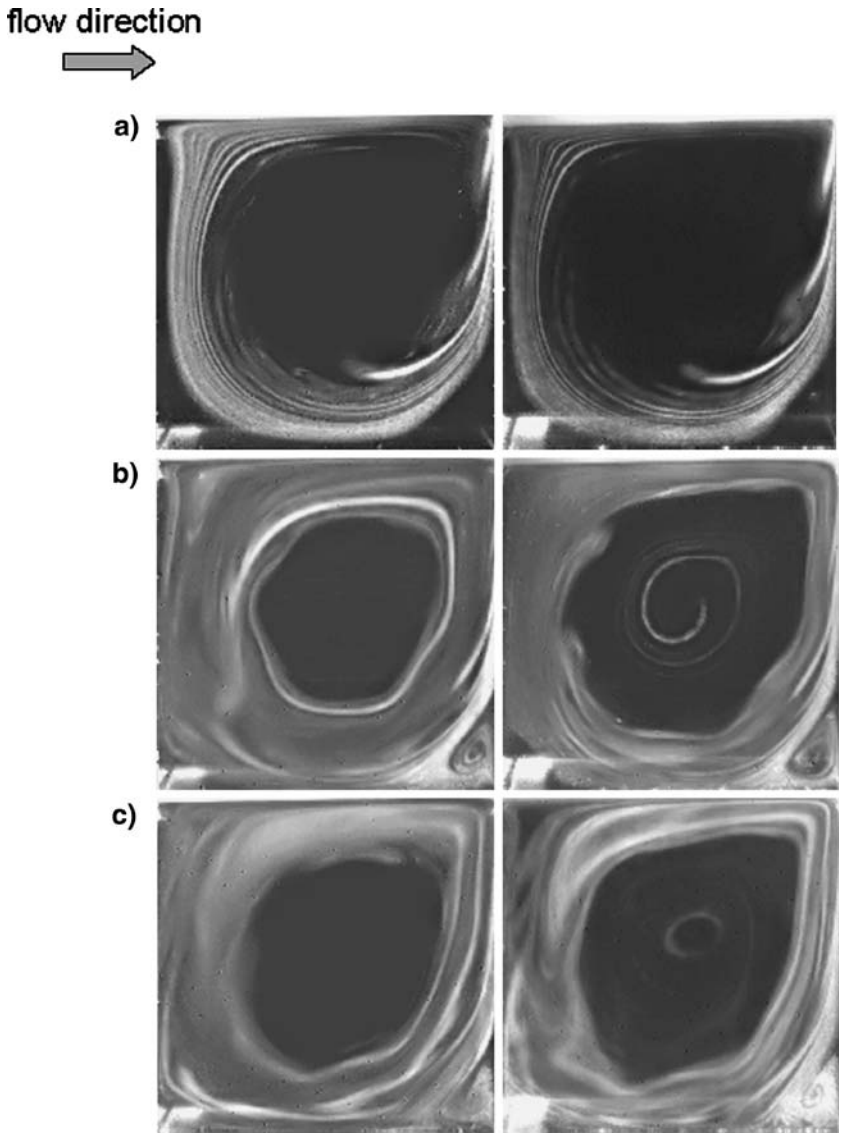

Fig. 10 Visualization in two parallel vertical planes (*left*: $z = 0$, *right*: $z = 30$ mm) for the same time and $R = 1$.
a $U_e = 0.69$ m/s ($Re = 2{,}300$)
b $U_e = 1.21$ m/s ($Re = 4{,}030$).
c $U_e = 1.60$ m/s ($Re = 5{,}330$)

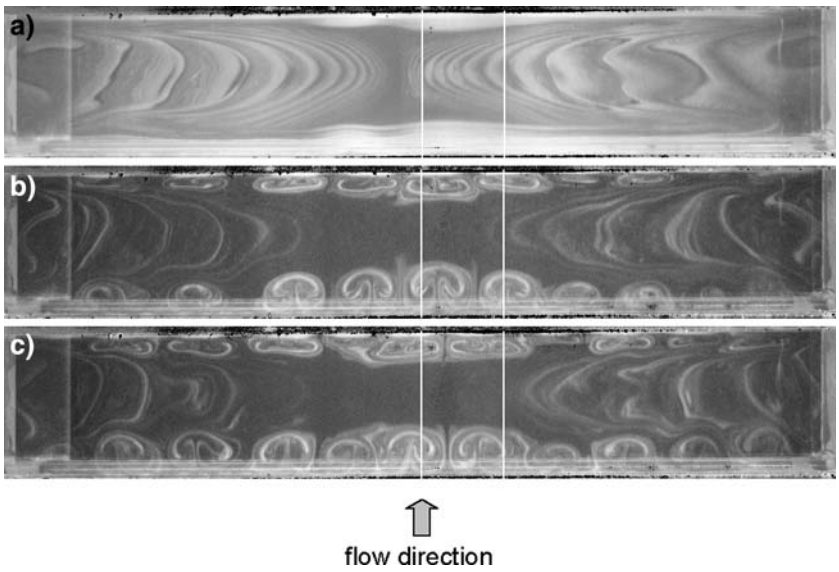

Fig. 11 Visualization in a horizontal plane for $R = 1$ and $y = -15$ mm.
a $U_e = 0.69$ m/s ($Re = 2{,}300$).
b $U_e = 1.21$ m/s ($Re = 4{,}030$).
c $U_e = 1.60$ m/s ($Re = 5{,}330$)

closed loop around the main vortex that would be cut by the laser plane. Note that the downstream part of the structure is much more flattened because of the shear layer injection inside the cavity. These vortices are not identified for velocity below $U_e = 1.21$ m/s. The inner part of the cavity shows a spanwise flow, coming from the cavity sides toward the centerline. The view in a transverse plane (Fig. 12) also exhibits these mushroom-like vortex patterns.

Figure 13 is a sketch of the flow for $R = 1$. The secondary vortex is nothing else but a corner vortex limited to the upstream wall bottom. Görtler-like vortices are present and the turbulence level is similar to what was observed on the tracer lines diffusion for $R = 1.5$. As the shear layer oscillations have little influence, the cavity flow is much similar to a lid-driven cavity flow (Koseff and Street 1984; Migeon 2002). Section 4 will come back to a deeper discussion of the Görtler-like vortices properties.

3.4 Aspect ratio $R = 0.5$

The flow dynamics drastically changes for $R = 0.5$. The seeding of the cavity by the external flow is very low and the injection volutes keep their consistence inside the cavity. The flow is purely laminar as there is no diffusion of the flow patterns. For $U_e = 0.69$ m/s (Fig. 14a), there is a vortex in the upper half of the cavity and no lower vortex is identified. This may be due to the absence of seeding or to the presence of a spanwise flow developing in the lower cavity half. For higher velocities (Fig. 14b, c), two counter-rotating vortices are developing along the cavity height. In fact, the lower vortex is seeded by the shear layer injection, and develops a spiraling pattern, while the upper vortex seeding is mainly provided by smoke diffusion. A spanwise flow may exist inside the vortices cores but is not clearly identified because of the lack of seeding.

The two white lines are the vertical visualization planes for $z = 0$ and $z = 30$ mm (Fig. 15). There is no more Görtler vortices generation (Figs. 15 and 16) but a slow diffusive-type spanwise motion. In the lower part of the cavity (Fig. 16), the span modulation of the smoke lines shows the transverse oscillation of the lower cavity vortex, and the associated core spanwise flow.

Figure 17 sketches the flow for $R = 0.5$. For the low velocities, there is a vortex limited to the upper half of the height, with no lower vortex or a spanwise flow below. For the higher velocities, there is a stack of two

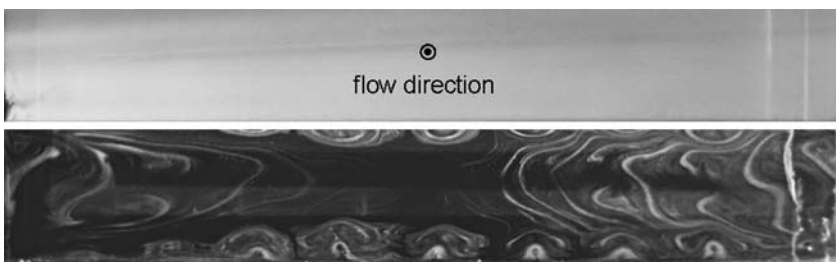

Fig. 12 Visualization in a transverse plane for $R = 1$, $U_e = 1.21$ m/s ($Re = 4{,}030$) and $x = L/2$

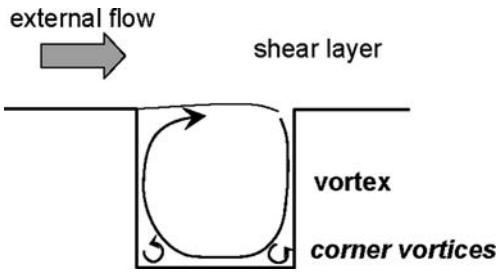

Fig. 13 Sketch of the cavity flow dynamics for $R = 1$

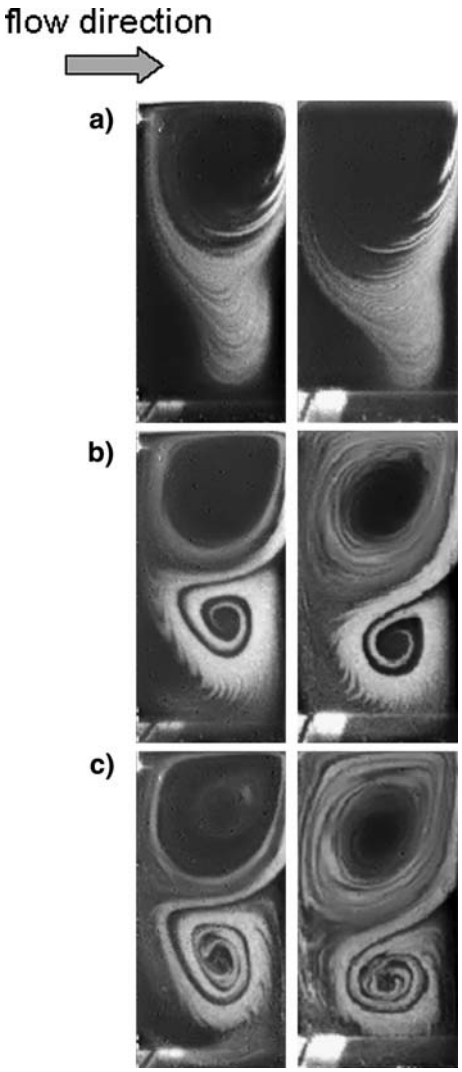

Fig. 14 Visualization in two parallel vertical planes (*left*: $z = 0$, *right*: $z = 30$ mm) for the same time and $R = 0.5$. **a** $U_e = 0.69$ m/s ($Re = 1{,}150$). **b** $U_e = 1.21$ m/s ($Re = 2{,}020$). **c** $U_e = 1.60$ m/s ($Re = 2{,}670$)

counter-rotating vortices. This behavior is alike the flow inside a lid-driven cavity, with no much influence of the shear layer dynamics.

4 Görtler vortices

The longitudinal vortices developing on a concave wall are subject to a linear stability mechanism as suggested by H. Görtler in Gottingen in 1940. The transverse positioning in pairs of the counter-rotating mushroom-like cells observed at the bottom of the cavity near the upstream wall for $R = 1$ and 1.5 (Figs. 11b, c and 8) is suggesting a development of Görtler-like vortices. In the present case, the flow curvature is caused by the main vortex. That hypothesis is consistent with quantitative results on the spanwise primary instability (Swearingen 1987). The Görtler number, defined from the curvature radius r_c, the kinematics viscosity of the fluid v and the velocity inside the cavity U_c developing away from the boundary layer of momentum thickness δ_2 is:

$$G\ddot{o} = \frac{U_c \delta_2}{\nu}\left(\frac{\delta_2}{r_c}\right)^{1/2}.$$

The dimensionless coefficient λ is built from the transverse wavelength λ, measured as the distance between a pair of two vortices:

$$\Lambda = \frac{U_c r_c}{\Lambda}\left(\frac{\lambda}{r_c}\right)^{3/2}.$$

The wave number k is defined as:

$$k = \frac{2\pi}{\lambda}.$$

It is associated with the wavelength λ to get a dimensionless wave number $k\delta_2$. This is leading to the Görtler number expression:

$$G\ddot{o} = \frac{\Lambda}{(2\pi)^{3/2}}(k\delta_2)^{3/2}.$$

For $R = 1$ the orders of magnitude can be estimated from flow visualizations. The wavelength λ is the distance between two pairs of structures measured in Fig. 11b, U_c is an estimate of the main vortex convection velocity inside the cavity and δ is an estimate of the boundary layer thickness inside the cavity determined from the displacement of a smoke mark in two successive images in a vertical plane, and r_c is the radius of curvature of the main vortex. The kinematics viscosity for the air is $v = 15 \times 10^{-6}$ m^2/s. The flow inside the cavity is laminar, the maximum Reynolds number calculated with the velocity U_c is 370, and, from the Blasius theory, the momentum thickness δ_2 is calculated from the relationship $\delta_2 = \delta/7.4$ with δ the

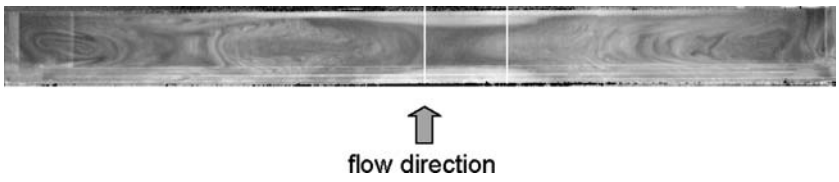

Fig. 15 Visualization in a horizontal plane for $R = 0.5$, $U_e = 1.21$ m/s ($Re = 2{,}020$) and $y = -15$ mm

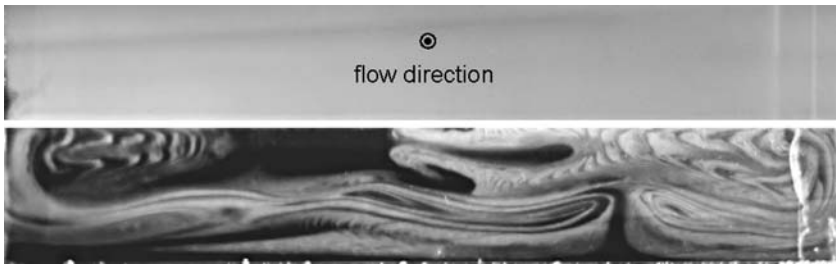

Fig. 16 Visualization in a transverse plane for $R = 0.5$, $U_e = 1.21$ m/s ($Re = 2{,}020$) and $x = L/2$

boundary layer thickness inside the cavity obtained from views in parallel planes. The measured data are presented in Table 1. Reporting the Görtler number versus the dimensionless wave number $k\delta_2$ on the stability diagram (Fig. 18) we observe a good agreement between our estimates and previous measurements. The experimental points, for a particular measurement, establish lines of constant slope 3/2, along which the non-dimensional wavelength is constant. Comparison is made with the neutral stability curves of Floryan and Saric (1982) and Hall (1983). Note that the present investigation has been obtained for much smaller curvature radii and velocities than the other ones (Tani 1962; Bippes 1972; Winoto and Crane 1980).

Now let us discuss some features of the Görtler-like vortices, postponing a more detailed analysis of their properties to a further work. First of all, it must be noticed that such longitudinal vortices are the most robust when only one main vortex exists within the cavity. Indeed, as soon as the secondary vortex appears, the Görtler-like vortices are stretched and dislocate. This is suggesting that the cavity aspect ratio range of their existence should be narrow around $R = 1$. For $R = 2$, the spanwise structures in the lower part of Fig. 4 must be thought as Görtler-like vortices, but they are very unsteady and it is difficult to measure a wavelength. Moreover these structures are continuously destroyed by the relatively high turbulence level inside the cavity.

Another interesting feature lays in the fact that the Görtler-like vortices raw, as seen in Figs. 11b, c and 12, is not stationary. To quantify their dynamical properties, we have plotted in Figs. 20 and 21, space–time diagrams of the pattern. Space–time diagrams are made by stacking over each other in Fig. 20b–d (respectively, in Fig. 21b–d) the single white line plotted in Fig. 20a (respectively, in Fig. 21a), at different successive times. These images are recorded in time with the set-up detailed in Fig. 2b. Time delay between two such lines is 50 ms. Total recording time along the vertical axis is 25 s. Time is passing from the bottom to the top, while the horizontal axis is the transverse z direction. The gray level in the diagrams corresponds to intensity variations along the extracted horizontal line. On such diagrams, vertical lines are associated to stationary events, while oblique lines are associated to traveling patterns. If oblique lines are moreover straight lines, it means that the pattern is traveling at a constant velocity $c = \Delta y/\Delta t$. Figure 20

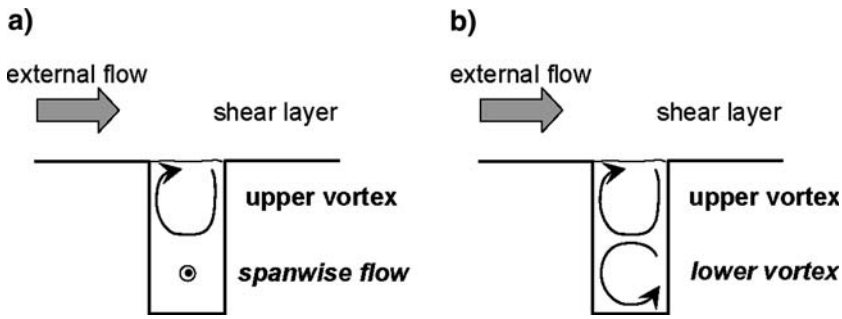

Fig. 17 Sketch of the cavity flow dynamics for $R = 0.5$. **a** for $U_e = 0.69$ m/s ($Re = 1{,}150$), **b** for $U_e = 1.21$ m/s ($Re = 2{,}020$) and $U_e = 1.60$ m/s ($Re = 2{,}670$)

Table 1 Parameters for the calculation of the Görtler number and the dimensionless wave number for $R = 1$

U_e (m/s)	λ (10^{-2} m)	U_c (m/s)	r_c (10^{-2} m)	δ (10^{-2} m)	δ_2 (10^{-3} m)	$G\ddot{o}$ (-)	Λ (-)	$k\,\delta_2$ (-)
1.21	2.95	0.1	2.5	1.5	2.03	3.85	214	0.456
1.6	2.6	0.105	2.5	1.5	2.03	4.04	186	0.517
2.09	2.2	0.11	2.5	1.5	2.03	4.23	151	0.611

exhibits the space–time behavior of the Görtler vortices raw located upstream inside the cavity and Fig. 21 the raw located downstream inside the cavity. In each one of these figures, the space–time diagrams are plotted for three different external velocities (b $U_e = 0.89$ m/s, c 1.21 m/s and d 1.595 m/s). The observation of these space–time diagrams leads to the following comments:

1. The Görtler vortices are not stationary as soon as they appear, for $U_e > 0.89$ m/s (Fig. 20b–d). There is a drifting symmetry with respect to the centerline. The left part of the raw is drifting to the left (left side of Fig. 20c), the right part is drifting to the right (right side of Fig. 20c). As a consequence, there appears a source-like singularity in the vortex raw, where there is a collision between a domain of left-traveling vortices to the left, and a domain of right-traveling vortices to the right. There, two adjacent vortices drift into two different directions (left vortex to the left, right vortex to the right) emptying an area in between which a new pair of vortices can nucleate. Let us remark that although source-like singularities exist with well-defined properties in the frame of non-linear traveling waves (Van Hecke et al. 1999; Pastur et al. 2003), the term ''source'' should be considered here in a very general context. Indeed, the ''source'' observed here seems to be induced by a secondary side flow symmetrical with respect to the centerline. This side flow, turned from the centerline toward the sides of the cavity, is expected to be forced by the inner spanwise flow coming from the cavity sides toward the centerline (Fig. 19), as previously reported (Migeon 2002).
2. The vortices drift over space with an increasing velocity with respect to their distance to the centerline. Such an increase of the velocity seems however not to be related to an increasing vortex amplitude, since on the very right side of the picture the vortices are evanescent and still drifting with the highest velocity. Drifting velocities reach a maximum value $c_{max} \sim 8.5$ mm s^{-1}.

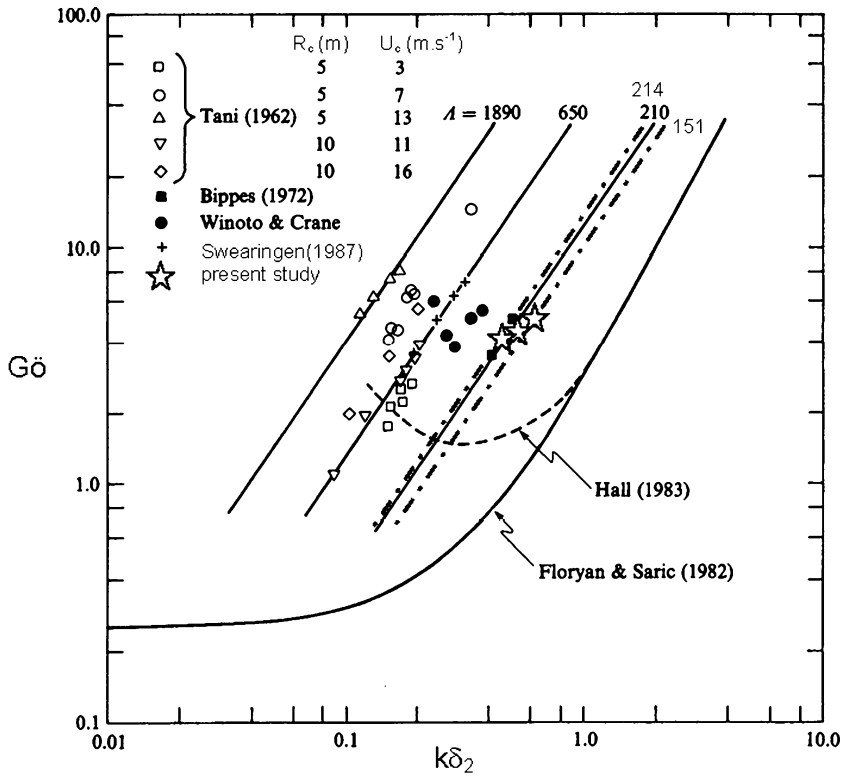

Fig. 18 Görtler number versus the dimensionless wave-number for previous studies and present measurements at $R = 1$

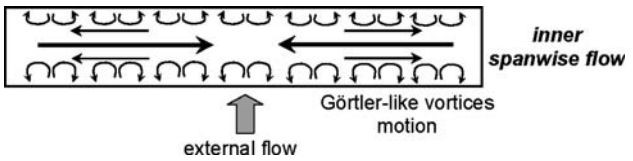

Fig. 19 Sketch of the flow dynamics and Görtler-like vortices motion for $R = 1$

3. Finally, when comparing the space–time diagrams obtained in the upstream (Fig. 20) and the downstream (Fig. 21) parts of the cavity, both patterns appear to be amazingly similar for $U_e > 0.89$ m s^{-1}. Such a strong correlation may not be due to chance. It instead confirms the annular shape of the Görtler-like vortices. It moreover indicates how strong and coherent their shape remains over space against any perturbation that the incoming flow may produce, although, from Figs. 20a or 21a, it is obvious that the downstream part of the Görtler vortices is strongly flattened compared with its upstream part.

For $R = 1$, before any increase of U_e the wind tunnel velocity was first brought to very high values so as to blow the smoke out of the cavity. It is strongly believed that such an operation may destroy the Görtler raw. Moreover after varying the aspect ratio ($R = 1.25$, Fig. 22), we recover a very similar space–time pattern of the Görtler raw. Therefore the reproducibility of the raw slowly drifting dynamics strongly suggests the existence of a secondary flow, symmetrical with respect to the centerline. In particular, a fruitful comparison could be done with the flow characteristics of Görtler-like vortices observed behind a backward facing step (Beaudoin et al. 2004).

5 Conclusion

Visualizations of the flow inside a rectangular cavity with aspect ratio varying between 0.5 and 2 have been conducted for $1{,}150 \leq Re \leq 10{,}670$. Three-dimensional spanwise structures are developing. The analysis of visualization time course of the flow shows that 3-D developments are not caused by shear layer secondary instabilities, as the latter remains rather a 2-D phenomenon. The study of the cavity flow with aspect ratio and Reynolds number has shown three morphological behaviors. For this range, the Reynolds number has little influence on that global flow morphology.

For $R = 2$, the flow is driven by the interaction between the shear-layer and the downstream wall. The injection inside the cavity is a rather 2-D phenomenon, creating a strongly unsteady main vortex in the downstream half of the cavity. A counter-rotating secondary vortex is size-modulated near the bottom upstream wall, and an induced flow is due to the motion of the two vortices, which is evolving in a spanwise flow. The presence of a secondary vortex in the upstream part of the cavity, linked with the unsteadiness of the main vortex, is opposing to the birth of the Görtler instabilities or is perturbating them.

The same global features are found for $R = 1.5$ with a lower turbulence level.

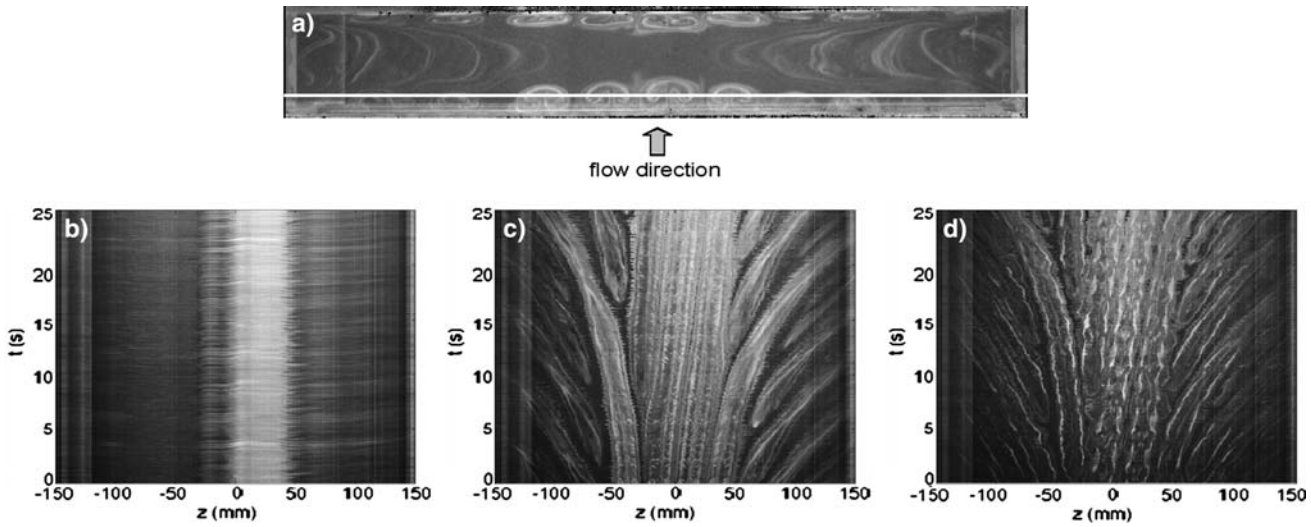

Fig. 20 **a** Visualization for $R = 1$, $U_e = 1.21$ m/s and $y = -15$ mm with the upstream white line used for the making of space–time diagrams. **b** Space–time diagram for $U_e = 0.89$ m/s ($Re = 2{,}970$). **c** Space–time diagram for $U_e = 1.21$ m/s ($Re = 4{,}030$). **d** Space–time diagram for $U_e = 1.6$ m/s ($Re = 5{,}330$)

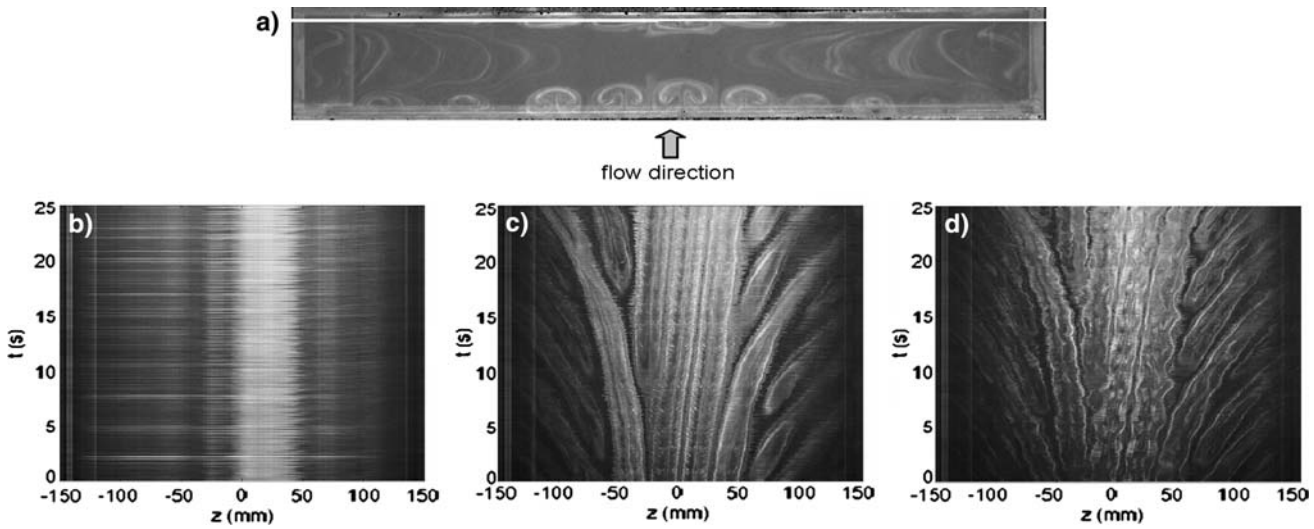

Fig. 21 **a** Visualization for $R = 1$, $U_e = 1.21$ m/s and $y = -15$ mm with the downstream white line used for the making of space–time diagrams. **b** Space–time diagram for $U_e = 0.89$ m/s ($Re = 2{,}970$). **c** Space–time diagram for $U_e = 1.21$ m/s ($Re = 4{,}030$). **d** Space–time diagram for $U_e = 1.6$ m/s ($Re = 5{,}330$)

For $R = 1$, the main vortex occupies the entire length of the cavity, and the secondary upstream vortex is reduced to a corner vortex. The main vortex boundary is time-evolving, as one can see in Fig. 10b with a small core associated with a large periphery for $z = 0$ and a larger core associated with a smaller periphery for $z = 30$ mm. There is also counter-flow acting in the core of the main vortex, from the cavity sides toward the symmetry plane, providing a seeding inside the cavity. The Görtler-like vortices migrate from the flow center of symmetry toward the cavity span sides. This motion is likely due to the spanwise flow acting in the periphery of the main vortex, from the center to the cavity sides (Migeon 2002).

For $R = 0.5$, there are two superimposed vortices, with a very low velocity and a purely laminar flow inside the cavity.

The Görtler-like vortices range of existence and dynamics will be further discussed in a forthcoming paper.

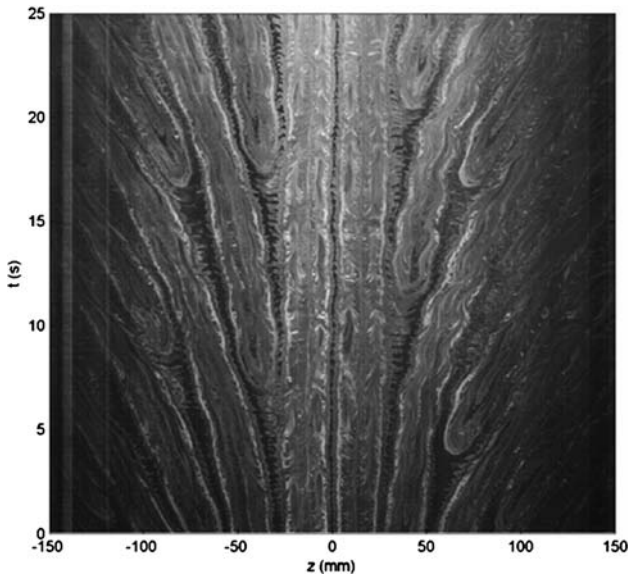

Fig. 22 Space–time diagram for $R = 1.25$ and $U_e = 1.21$ m/s ($Re = 5{,}042$)

References

Beaudoin JF, Cadot O, Aider JL, Weisfreid JE (2004) Three-dimensional stationary flow over a backward-facing step. Eur J Mech B Fluids 23:147–155

Bilanin AJ, Covert EE (1973) Estimation of possible excitation frequencies for shallow rectangular cavities. AIAA J 11(3):347–351

Bippes H (1972) Experimentelle Untersuchung des laminar-turbulenten Umschlags an einer parallel angeströmten könkaven Wand. Heidel. Akad. Wiss. Naturwiss. Kl. 3:103 (also NASA TM-75243, 1978)

Chang CH, Meroney RN (2003a) The effect of surroundings with different separation distances on surface pressures on low-rise buildings. J Wind Eng Ind Aerodyn 91:1039–1050

Chang CH, Meroney RN (2003b) Concentration and flow distributions in urban street canyons: wind tunnel and computational data. J Wind Eng Ind Aerodyn 91:1141–1154

Chatellier L, Laumonier J, Gervais Y (2004) Theoretical and experimental investigations of low Mach number turbulent cavity flows. Exp Fluids 36:728–740

Chung KM (2001) Three-dimensional effect on transonic rectangular cavity flows. Exp Fluids 30:531–536

Dezsö-Weidinger G, Stitou A, Van Beeck J, Riethmuller ML (2003) Measurements of the turbulent mass flux with PTV in a street canyon. J Wind Eng Ind Aerodyn 91:1117–1131

Fang LC, Nicolaou D, Cleaver JW (1999) Transient removal of a contaminated fluid from a cavity. Int J Heat Fluid Flow 20:605–613

Floryan JM, Saric WC (1982) Stability of Görtler vortices in boundary layers. AIAA J 20(3):316–324

Forestier N, Jacquin L, Geffroy P (2003) The mixing layer over a deep cavity at high-subsonic speed. J Fluid Mech 475:101–145

Geveci M, Oshkai P, Rockwell D, Lin JC, Pollack M (2003) Imaging of the self excited oscillation of flow past a cavity during generation of a flow tone. J Fluids Struct 18:665–694

Gharib M, Roshko A. (1987) The effect of flow oscillations on cavity drag. J Fluid Mech 177:501–530

Ghia U, Ghia KN, Shin CT (1982) High-re solutions for incompressible flow using the Navier-Stokes equations and a multigrid method. J Comput Phys 48:387–411

Grace SM, Dewar WG, Wroblewski DE (2004) Experimental investigation of the flow characteristics within a shallow wall cavity for both laminar and turbulent upstream boundary layers. Exp Fluids 36:791–804

Guermond JL, Migeon C, Pineau G, Quartapelle L (2002) Start-up flows in a three-dimensional rectangular driven cavity of aspect ratio 1:1:2 at Re = 1000. J Fluid Mech 450:169–199

Hall P (1983) The linear development of Görtler vortices in growing boundary layers. J Fluid Mech 130:41–58

Heller HH, Bliss B (1975) The physical mechanism of flow-induced pressure fluctuations in cavities and concepts for their suppression. AIAA Paper 75–491, 2nd Aeroacoustics Conference, Hampton

Howe MS (2003) Mechanism of sound generation by low Mach number flow over a wall cavity. J Sound Vib 273:103–123

Huerre P, Rossi M (1998) Hydrodynamic instabilities in open flows. In: Godrèche C, Manneville P (eds) Hydrodynamics and nonlinear instabilities. Cambridge University Press, pp 81–294

Kegerise MA, Spina EF, Garg GS, Cattafesta LN III (2004) Mode-switching and nonlinear effects in compressible flow over a cavity. Phys Fluids 16(3):678–687

Komerath NM, Ahuja KK, Chambers FW (1987) Prediction and measurement of flows over cavities—a survey. AIAA Paper 87–0166

Koseff JR, Street RL (1984) Visualization studies of a shear driven three-dimensional recirculating flow. J Fluids Eng 106:21–29

Kuo CH, Chang CW (1998) Shear-layer characteristics across a cavity with a horizontal top plate. Fluid Dyn Res 22:89–104

Kuo CH, Jeng WI (2003) Lock-on characteristics of a cavity shear layer. J Fluids Struct 18:715–728

Larchevêque L, Sagaut P, Lê TH, Comte P (2004) Large-eddy simulation of a compressible flow in a three-dimensional open cavity at high Reynolds number. J Fluid Mech 516:265–301

Lin JC, Rockwell D (2001) Organized oscillations of initially turbulent flow past a cavity. AIAA J 39(6):1139–1151

Mendoza JM, Ahuja KK (1995) The effect of width on cavity noise. J Aircr 14(9):833–837

Migeon C (2002) Details on the start-up development of the Taylor-Görtler-like vortices inside a square-section lid-driven cavity for 1,000 ≤ Re ≤ 3,200. Exp Fluids 33:594–602

Migeon C, Pineau G, Texier A (2003) Three-dimensionality development inside standard parallelepipedic lid-driven cavities at Re = 1000. J Fluids Struct 17:717–738

Pastur L, Westra MT, Van de Water W (2003) Sources and sinks in 1D travelling waves. Physica D 174:71–83

Rockwell D (1983) Oscillations of impinging shear layers. AIAA J 21(5):645–664

Rockwell D, Naudascher E (1978) Review self-sustained oscillations of flow past cavities. J Fluids Eng 100:152–165

Rossiter JE (1964) Wind-tunnel experiments on the flow over rectangular cavities at subsonic and transonic speeds. Aeronautical Research Council Reports and Memoranda 3438

Rowley CW, Colonius T, Basu AJ (2002) On self-sustained oscillations in two-dimensional compressible flow over rectangular cavities. J Fluid Mech 455:315–346

Sarohia V (1977) Experimental investigation of oscillations in flows over shallow cavities. AIAA J 15(7):984–991

Swearingen JD, Blackwelder RF (1987) The growth and breakdown of streamwise vortices in the presence of a wall. J Fluid Mech 182:255–290

Tam CKW, Block PJW (1978) On the tones and pressure oscillations induced by flow over rectangular cavities. J Fluid Mech 89:373–399

Tani I (1962) Production of longitudinal vortices in the boundary layer along a concave wall. J Geophys Res 67:3075–3080

Umesh Chandra B, Chakravarthy SR (2005) Experimental investigation of cavity-induced acoustic oscillations in confined supersonic flow. J Fluids Eng 127:761–769

Van Hecke M, Storm C, Van Saarloos W (1999) Sources, sinks and wavenumber selection in coupled CGL equations and implications for counterpropagating wave systems. Physica D 134:1–47

Winoto SH, Crane RI (1980) Vortex structure in laminar boundary layers on a concave wall. Int J Heat Fluid Flow 2:221–231